Soft Matter

PAPER

View Article Online
View Journal | View Issue

Check for updates

Cite this: *Soft Matter*, 2021, 17, 8105

3D-Reactive printing of engineered alginate inks

Lorenzo Sardelli, Marta Tunesi, Francesco Briatico-Vangosa and Paola Petrini *

Received 23rd April 2021,
Accepted 23rd July 2021

DOI: 10.1039/d1sm00604e

rsc.li/soft-matter-journal

Alginate is a common component of bioinks due to its well-described ionic crosslinking mechanism and tunable viscoelastic properties. Extrusion-based 3D-printing of alginate inks requires additives, such as gelatin and Pluronic, pre- or post-printing crosslinking processes and/or coextrusion with crosslinkers. In this work, we aim to develop a different printing approach for alginate-based inks, introducing 3D-reactive printing. Indeed, the control over the crosslinking kinetics and the printing time allowed printing different inks while maintaining their final composition unaltered to identify a suitable formulation in terms of printability. Alginate solutions were crosslinked with insoluble calcium salts ($CaCO_3$) inducing a dynamic modification of their microstructure and viscoelastic properties over time. The monitoring of fiber printability and internal microstructure, at different time points of ink gelation, was performed by means of a well-defined set of rheological tests to obtain *a priori* ink properties for the *a posteriori* 3D-printing process. This new perspective allowed 3D-reactive printing of alginate fibers with predetermined properties, without involving post-extrusion crosslinking steps and additives.

Open Access Article. Published on 26 July 2021. Downloaded on 7/12/2024 3:28:43 AM.
This article is licensed under a Creative Commons Attribution-NonCommercial 3.0 Unported Licence.

Introduction

3D-printing technologies are spreading around the world, accelerating the development of various engineering sectors, such as artificial intelligence,[1] building construction,[2,3] food industry[4] and electrochemical applications.[5,6] The possibility to print complex geometries with high precision has made 3D-printing a particularly attractive tool in the field of bioengineering, leading to an enormous progress in the development of patient-specific prostheses,[7–10] *in vitro* models of complex biological systems[11–13] and constructs for tissue regeneration.[14–18] In these last fields, hydrogels of different origins are usually extruded from a needle or nozzle, thus forming fibers of variable size (from milli to micro) with the designed geometry.[19]

The capability of a material to be extruded in self-standing fibers with dimensions suitable for a specific application is defined as "printability".[20–22] The development of new inks for 3D-printing is a complex challenge as different parameters, such as the polymer type, concentration and degree of crosslinking, require efforts and time to be optimized in terms of printability.[19,23] To speed up this process, advanced rheological characterization techniques can be used to predict *a priori* the ink printability by analysing a few key features.[22] For instance, the viscosity profiles as a function of the applied shear rate and shear stress are the main properties interpreted, by means of theoretical models, in terms of useful post-printing features such as extrudability, stress distribution and capability to form self-standing fibers.[22,24,25] These techniques were used not only for a wide range of materials of artificial origin, such as PEG[26] and Pluronic F127,[27] but also for natural origin hydrogels like chitosan,[28] gelatin,[29,30] collagen,[31] alginate,[32] and composites.[33,34]

Among the different inks that were proposed for 3D-printing, alginate assumes a position of relevance for different reasons. This polysaccharide is well appreciated for the easily tunable properties, the cost effectiveness and the compatibility with the encapsulation/loading of cells and bacteria.[22,32] However, alginate solutions are not able to form stable 3D structures due to the viscous behavior that induces spreading of the printed structures.[22]

Possible methods to improve their printability are the use of support materials (*e.g.*, gelatin, Pluronic F127 and agar) or fillers (*e.g.*, ceramic fibers and nanoparticles). These supports are needed to obtain shape fidelity of alginate, which cannot produce self-standing fibers alone and without a crosslinking process post-extrusion. Moreover, these approaches rely on the concept that the composition of the hydrogels should be adapted to fit the needs of the 3D-printing process. This results in the production and characterisation of a range of candidate compositions to be compared and tested in quest of the optimal formulation.[34–36]

The 3D-printing of alginate solutions consists, typically, in ionic crosslinking of the polysaccharidic chains in the presence of divalent cations in solution.[32,37–39] In the majority of the applications, the ionic crosslinking is obtained by extruding the

Department of Chemistry, Materials and Chemical Engineering "Giulio Natta", Politecnico di Milano, Piazza Leonardo da Vinci 32, 20133 Milan, Italy.
E-mail: paola.petrini@polimi.it

Open Access Article. Published on 26 July 2021. Downloaded on 7/12/2024 3:28:43 AM.
This article is licensed under a Creative Commons Attribution-NonCommercial 3.0 Unported Licence.

alginate in Ca^{++}-enriched baths. In this case, the gelation (commonly defined as *external gelation*) of the polymeric chains is fast and confined at the interface between the alginate fibers and the crosslinking solution, drastically limiting fiber spreading but inducing a non-homogeneous gelation.[32] Calcium salts such as calcium chloride ($CaCl_2$) or calcium sulfate ($CaSO_4$) can also be used as pre-printing crosslinkers of the ink (*i.e.* pre-crosslinking) to enhance the hydrogel toughness during extrusion and, hence, to print fibers with higher shape maintenance.[40–42] As an alternative to soluble calcium salts as pre-printing crosslinkers, it is possible to induce an extremely homogeneous gelation by using insoluble calcium salts. In this case, crystals of calcium carbonate ($CaCO_3$) or calcium phosphate (CaP) are homogeneously suspended into the alginate solution and then solubilized by the addition of acidifying agents, usually glucono-δ-lactone (GDL).[43–46] The gradual dissolution of the calcium salts results in a progressive release of free Ca^{++} ions in the whole bulk of the solution over time. In this way, the formation of crosslinking sites among the polymeric chains is uniformly distributed, leading to the formation of an extremely homogeneous 3D network. Although the homogeneous gelation of alginate, defined as *internal gelation*, was actively exploited for microsphere formation, insulin encapsulation and drug delivery systems,[47–49] it is still poorly assessed for 3D-printing purposes, limiting its few applications in pre-crosslinking treatment as an alternative to $CaCl_2$ or $CaSO_4$.[41,44,50]

The current strategies for alginate 3D-printing shared common limitations independently of the specific application. For example, the interfacial ionic crosslinking induced by soluble calcium salts led to only homogeneous fibers with complex and not-user-friendly setups and long optimization processes.[22,42,51–55] This inhomogeneity exerted both direct and indirect effects on the cells. The direct effect is attributed to the microstructural gradient due to the external gelation generating a non-uniform distribution of cells along the fiber section.[22,42,56,57] Although it may not be considered a disadvantage *per se*, inhomogeneity is not tunable *a priori* when state-of-the-art 3D-printing approaches are used, where it can only be considered as experimental evidence to be observed after the ink optimization steps. In addition, the higher ionic-crosslinking degree on the external surface of the fiber indirectly influences the cellular behavior by limiting the diffusion of molecules, such as oxygen and nutrients.[22,58]

The internal microstructure of the fiber, which can be characterized by the dimension of the polymeric network constituting the ink, surprisingly remains poorly investigated in the field of 3D-printing. To the authors' knowledge, no studies focusing on the internal microstructure of the fibers were conducted, although this knowledge could support the development of models to predict the diffusion of molecules, such as oxygen and glucose, but also specific cellular parameters, such as their mobility, as already reported in studies with other purposes.[59–61]

Regardless of the type of gelation (*i.e.*, internal or external) used to pre- or post-crosslinking alginate, the inks for 3D-printing are, at date, obtained after a complex trial and error approach, which aims at optimizing their composition. The initial composition needs to be modified until optimized printability-related parameters are obtained. This approach implies two main consequences. First, the "process" is dependent on the "result" and, hence, it deviates from the standardization scope that is a priority in the engineering perspective. Indeed, when an engineering approach is assessed, the control over the process should guarantee results that are dependent on the parameters of the process itself, and not *vice versa*. Second, printability is considered as a fixed property over time, uniquely associated with a defined ink composition that does not change. Consequently, when a certain composition is optimal for a specific application but not printable, it is necessary to change the ink features to improve printability, even though this may entail a deviation from the optimal functionality for the final use (for example, the *in vitro* modelling of tissues mechanical properties).

This work intends to push further these well-characterized methods of printing alginate in 3D. In particular, the main characteristics of internal gelation, which are the dynamic variation of the viscoelastic properties and the homogeneous network formation, will be used for the ink optimization. We named this new approach "3D-reactive printing" to underline the transient nature of the reacting mixture during the printing process, which is the peculiar feature of the proposed approach. We selected "reactive" as "the term expressing a kinetic property".[62] The control over the printing time will be assessed as a new key factor to be considered when optimizing the ink printability. For these reasons, rheological characterization will be performed during the dynamics of internal gelation and used to tune the viscoelastic features related to printability (*i.e.*, shear thinning behavior, yield stress and recovery). The approach discussed in this work, defined as reactive printing, is investigated as a new strategy to modify the printability of alginate hydrogels without varying their composition.

Materials and methods

Materials

The different inks were produced with alginic acid sodium salt (Sigma-Aldrich 180947; Lot MKBZ9710V), sodium chloride 99.0–100.5% (NaCl) (Sigma-Aldrich; Lot 13423), calcium carbonate $\geq$ 99.0% ($CaCO_3$) (Sigma-Aldrich C4830; Lot SLBL4279V) and D-(+)-gluconic acid δ-lactone (GDL) (Sigma-Aldrich G4760; Lot SLBM7762V). For the complete DMEM formulation, Dulbecco's Modified Eagle Medium, foetal bovine serum (FBS), L-glutamine and penicillin–streptomycin solution were purchased from Sigma-Aldrich.

Ink preparation

Alginate inks were prepared by using either saline solution (0.057% w/v NaCl concentration) (S-ink) or complete DMEM medium (enriched with 10% FBS, 2 mM L-glutamine, 100 U mL^{-1} penicillin and 100 $\mu g\ mL^{-1}$ streptomycin) (D-ink). Alginate powder was dissolved in the solvents by gently stirring for at least 12 h at room temperature. The solutions were mixed in volume ratios of 1 : 5 and 1 : 6, respectively, with 2% (w/v) $CaCO_3$ suspension and 7 or 20% (w/v) GDL solution (in the case of saline solution or

 This journal is © The Royal Society of Chemistry 2021

Open Access Article. Published on 26 July 2021. Downloaded on 7/12/2024 3:28:43 AM. This article is licensed under a Creative Commons Attribution-NonCommercial 3.0 Unported Licence.

complete DMEM, respectively). The mass of alginate was set to reach a final concentration of 4.5% (w/v). For the rheological characterization, alginate hydrogels (2 mL) were poured into Petri dishes (diameter of 35 mm) to obtain samples with a thickness of ~2 mm. For the printing process, the alginate hydrogels (3 mL) were immediately poured into cartridges (CELLINK, Gothenburg, Sweden).

Rheological characterisation

Time sweep scans in oscillations, steady state rotational rheometry under shear and recovery tests were performed with a rotational rheometer (Anton Paar, Modular Compact Rheometer MCR 502) in a parallel plate configuration with 25 mm diameter plates (Anton Paar, serial number: 52 890). The tests were carried out at 25 °C, while controlling the temperature using a Peltier system.

After ensuring that no slip was occurring, the gap was always set at 0.5 mm.

The time sweep test was performed immediately after the ink preparation. The test duration was 3 h, during which a sinusoidal shear strain history, with a 0.5% amplitude and a frequency of 1.0 Hz, was applied.

After the time sweep test, the flow behavior of the inks was investigated immediately (0 min) and 30 min after the preparation by applying a shear rate ranging from 0.01 s^{-1} to 2000 s^{-1}.

Furthermore, the presence of a yield stress of the inks at 0, 30, 60 min and 24 h after preparation was investigated by means of shear stress amplitude sweep in oscillation with amplitude ranging from 0.1 to 100 Pa at a constant frequency of 1 Hz.

The viscosity recovery measurements were performed at 0 min and 30 min by applying a low shear rate of 0.01 s^{-1} for 200 s, followed by a high shear rate window (100 s) at 895 s^{-1} and a final low shear rate window of 0.01 s^{-1} (starting at 200 s). Similarly, the recovery in the oscillatory regime was obtained by measuring the storage (G') and loss (G'') moduli, for all the time points considered, at three strain amplitudes (0.5%, 100% and again 0.5%), maintained for 100, 100 and 200 s, respectively, and a constant frequency of 1 Hz.

The G' and G'' of the inks at 0 min, 30 min, 60 min and 24 h were measured in the frequency range of 0.1–20 Hz with an applied shear strain of 0.5% (frequency sweep test).

Microstructural characterization of the inks

The frequency response of the viscoelastic properties was interpreted by applying the Generalized Maxwell Model (GMM) to estimate the microstructural evolution of the inks during the gelation process.

The microstructure was described in terms of the mesh size, ξ, corresponding to the distance between two crosslinking sites on the same alginate chain. In a bioengineering application this parameter is useful both to compare the structure of the hydrogel with that of the tissue to be modeled and to predict the diffusivity through the hydrogel (considering only the steric interaction).[63–65]

The data were obtained in the linear viscoelastic regime and could be interpreted by applying the GMM, which consist of n Maxwell elements connected in parallel. Each element is formed by one spring (elastic component) and one dashpot (viscous component) connected in series, which are characterized, respectively, by a specific relaxation time, λ_i, and viscosity, η_i. The elements are then connected in parallel. Similarly to other studies, the relaxation times of the springs were considered scaled each other by a factor of 10 (*i.e.*, $\lambda_i = 10{\cdot}\lambda_{i+1}$) and a pure elastic element (spring with relaxation time G_e) was added in parallel to the other Maxwell elements.[63,64,66,67]

From the GMM, it is possible to predict the dependence of G' and G'' on frequency (eqn (1) and (2)):

$$G' = G_e + \sum_{i=1}^{n} G_i \frac{(\lambda_i \omega)^2}{1 + (\lambda_i \omega)^2}; \quad G_i = \frac{\eta_i}{\lambda_i} \tag{1}$$

$$G'' = \sum_{i=1}^{n} G_i \frac{(\lambda_i \omega)^2}{1 + (\lambda_i \omega)^2}; \quad G_i = \frac{\eta_i}{\lambda_i} \tag{2}$$

where ω is the angular frequency, and η_i and λ_i are the viscosity and relaxation time associated to the i-th Maxwell element, respectively. These equations were not applied for the time points of the crosslinking kinetics that preceded the gel point, as no network is present, but only for those that satisfied the condition $G' > G''$ (*i.e.*, solid-*like* behavior).

To estimate the microstructure of the inks, the GMM was used to fit the frequency sweep curves by minimizing the error, defined according to eqn (3), between the theoretical results and experimental data:

$$\text{error} = (n + 2){\cdot}\chi^2 \tag{3}$$

where χ^2 is the Chi-squared error, n is the number of Maxwell elements which varies from 1 to 10, and $n + 2$ is the number of parameters describing the GMM.

The theoretical G_e and G_i obtained by the fitting (eqn (1) and (2)) can be combined to obtain the fully relaxed shear modulus (G_∞) in the form of eqn (4):

$$G_\infty = G_e + \sum_{i}^{n} G_i; \quad G_i = \frac{\eta_i}{\lambda_i} \tag{4}$$

where n is the optimized number of Maxwell elements fitting the frequency curves. The shear modulus can be further related to the microstructure of the material using the theory of rubber elasticity according to eqn (5):

$$\xi = \sqrt[3]{\frac{6RT}{\pi N_A G_\infty}} \tag{5}$$

where R is the universal gas constant, T the absolute temperature, Na the Avogadro constant and ξ is the estimated mesh size, corresponding to the mean distance between two crosslinking sites on the same polymer chain.

Printing process and printability evaluation

The inks were printed at different time points using a CELLINK INKREDIBLE+ bioprinter, an extrusion-based bioprinter with a driving force provided by air compression. The structure to be printed was first described in the predefined code of Repetier-Host (Hot-World GmbH & Co. KG, Willich, Germany). The code

Open Access Article. Published on 26 July 2021. Downloaded on 7/12/2024 3:28:43 AM.
This article is licensed under a Creative Commons Attribution-NonCommercial 3.0 Unported Licence.

was operated by Slic3r to create the geometry-code (G-code) file containing the specific fill density, fill pattern, layer dimension, as well as other printing parameters. For the evaluation of the fiber dimension, a 130 × 130 mm^2 grid (infill: 10%) was selected as the printing geometry with a fiber distance of 40 mm. After loading the cartridge with the ink (2.5 mL in 5 mL syringes), the minimal pressure for extrusion was identified as the pressure at which a continuous flow of material started to be observed from the nozzle tip (nominal internal diameter of 0.250 mm). This pressure was also increased in steps of 2 kPa to investigate, in the same printing process, the variation of the fiber diameters as a function of the applied pressure.

The uniformity factor (U) of the fibers was determined by computing the ratio between the length of the fiber profile and the length of an ideal fiber with a perfectly straight profile (for interpretation of the parameters, see also Fig. 9). For fibers printed at the minimal pressure, the coefficient U was hence determined using the formula (eqn (6)):

$$U = \frac{L_{\text{real}}}{L_{\text{ideal}}} \tag{6}$$

The pore coefficient (P_r) and the perimeter coefficient (P_e) were computed by analyzing the pores and the perimeter of a bi-layered geometry of 20 × 20 × 0.5 mm^3 (infill: 25%) accordingly to eqn (7) and (8):

$$P_r = \frac{(\text{Pore perimeter})^2}{16 \cdot (\text{pore area})} \tag{7}$$

$$P_e = \frac{1}{\left\{\left[\frac{1}{2}\cdot\left(\frac{\overline{L_x}}{L_x}+\frac{\overline{L_y}}{L_y}\right)-1\right]+1\right\}\cdot\left[1+\frac{1}{2}\cdot\left(\frac{\sigma_x}{L_x}+\frac{\sigma_y}{L_y}\right)\right]} \tag{8}$$

where $\overline{L_x}$ and $\overline{L_y}$ are the mean lengths of the printed edges, σ_x and σ_y are their standard deviations and L_x and L_y are the theoretical lengths of the geometry (*i.e.*, 20 mm) along the horizontal and vertical axes, respectively. All the dimensional investigations were made using an optical microscope (Leica, DMi1 model) in inverted light mode with a 5× magnification. Data were analyzed using the free ImageJ software.

Statistical analysis

All the experiments were repeated at least in triplicate, with data expressed as mean ± standard deviation. For comparison, the normality test (D'Agostino–Pearson test) was performed to investigate Gaussian distribution. As a consequence of the normality test results, ANOVA or Kruskal–Wallis tests were used to compare groups, while *t*-test or Mann–Whitney test were used to compare two groups of data. The statistical analysis was performed using GraphPad Prism (GraphPad Software, Inc., CA, US), release 8.0.1.

Results

Rheological characterization

The time sweep test was performed to estimate the gel point of the 4.5% alginate inks by plotting the curves of G'', G' and their ratio (*i.e.*, loss factor, tan (δ)) over time (Fig. 1). The gel point is defined as the moment when the storage modulus is equal to the loss modulus (*i.e.*, when tan (δ) = 1) at the considered frequency. In the case of the inks in saline solution (S-ink) (Fig. 1A), the gel-point was reached 37 ± 4 min after the addition of the GDL solution to the alginate–$CaCO_3$ mixture, considered as the starting moment of the internal ionic-crosslinking (t = 0; pH 6.9). Similarly, the gel-point of the inks in complete DMEM (D-ink) was reached after 45 ± 3 min at pH 6.7 (Fig. 1B). Similar gel points for S-ink and D-ink were reached by increasing the GDL concentration to compensate for the differences in composition, including 1% w/v in D-ink (saline concentration in DMEM) and 0.057% w/v NaCl in S-ink (an arbitrarily selected physiological condition, *i.e.* the physiological concentration of NaCl in intestinal mucus). The other rheological tests were performed considering four different time points during the dynamics of the internal gelation: immediately after the preparation (0 min), before the gel-point (30 min, pH 6.4 for S-ink and pH 5.9 for D-ink), after the gel-point (60 min, pH 6.3 for S-ink and pH 5.8 for D-ink) and at complete gelation (24 h, pH 6.1 for S-ink and pH 4.1 for D-ink). The definition of the gel point allowed recognition of the timeframes when the inks behaved more like a liquid or a solid material (before and after the gel point, respectively).

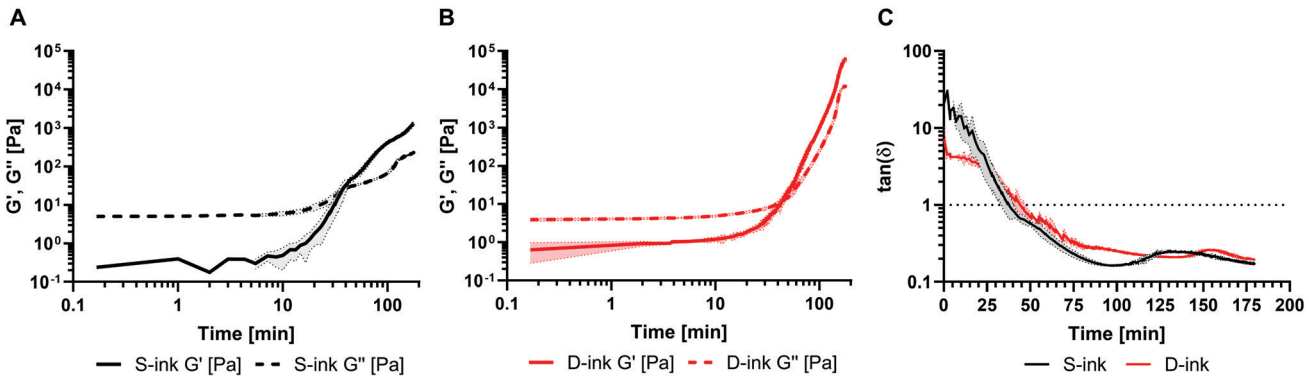

Fig. 1 The kinetics of the homogeneous crosslinking of the inks in saline (A, black lines) and DMEM (B, red lines) expressed by measuring G'' (dashed line) and G' (continuous line) or considering their ratio tan (δ) (C) over time.

 This journal is © The Royal Society of Chemistry 2021

Open Access Article. Published on 26 July 2021. Downloaded on 7/12/2024 3:28:43 AM.
This article is licensed under a Creative Commons Attribution-NonCommercial 3.0 Unported Licence.

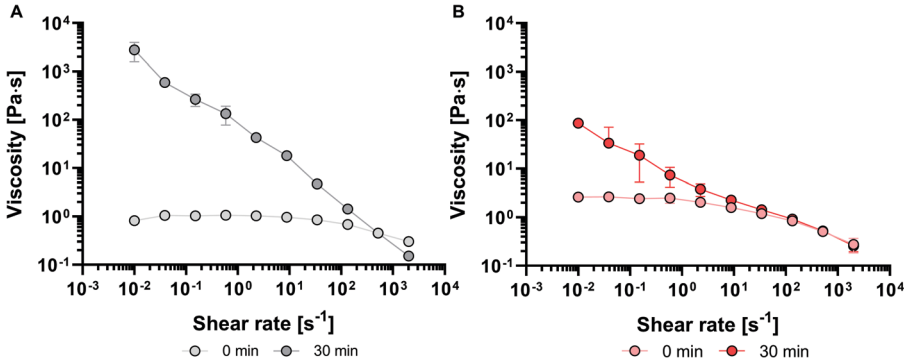

Fig. 2 Viscosity curve as a function of the shear rate for S-ink and D-ink (A and B, respectively) at the time points of their liquid-*like* behavior, *i.e.* 0 and 30 min (clearer and darker colors, respectively).

The shear viscosity was acquired for inks in the liquid-*like* state by the flow measurements at variable shear rates (Fig. 2). Immediately after preparation (t = 0 min), the S-ink showed an almost constant viscosity as a function of the shear rate, which corresponds approximately to an ideal Newtonian fluid. Differently, the viscosity of the just prepared D-ink slightly decreased while increasing the shear rate, displaying a slight shear thinning behavior. After 30 min, the inks displayed shear thinning behavior independently of the solutions used for the preparation. At lower shear rates, the differences in viscosity between the S-ink and D-ink were more evident with time, with S-ink showing higher values. These differences reduced at higher shear rates, when the shear thinning behavior implied a viscosity decay reaching values similar to those measured immediately after GDL addition.

The estimation of the shear thinning behavior at 30 min was obtained by fitting the curves with the power law regression (eqn (7)):

$$\eta = K(\dot{\gamma})^{n-1} \quad (9)$$

where η is the viscosity, $\dot{\gamma}$ the shear rate, K the flow consistency index and n the flow behavior index (Table 1).

A shear stress amplitude sweep in oscillation was run to get the shear stress at which the material started flowing, *i.e.* that causing a transition from a solid-*like* condition to a liquid-*like* one (from $\tan(\delta) < 1$ to $\tan(\delta) > 1$). The S-ink and D-ink exhibited similar trends over time, with no yield found at 0 and 30 min as no solid-*like* behaviour ($\tan(\delta) < 1$) was observed. For the other time points, the yield-stress of D-ink and S-ink increased with the crosslinking time, being minimum at 60 min and maximum after 24 h (Table 2). The yield stress values of D-ink after 60 min and 24 h were comparable to those found for S-ink.

The S-ink and D-ink in their liquid-*like* state (0 and 30 min) were subjected to a shear rate history comprising a lower shear rate, followed by a step increase in this variable and then by a decrease to the initial value. The first step aims at simulating the low shear experienced by the ink before extrusion, while the second and third steps modelled the flow condition in the nozzle tip during extrusion and the post-printing state, respectively (Fig. 3). Immediately after preparation, either the S-ink or D-ink was not able to completely recover the original viscosity after the simulated extrusion condition, as the curves described a viscosity decrease of 25% (S-ink) and 18% (D-ink). Differently, the viscosity loss measured after the higher shear rate window was drastically reduced 30 min after preparation (5 and 6% for the S-ink and D-ink, respectively). However, the recovery was not immediate, but required ~140 s for S-ink and ~90 s for D-ink to reach 95% of the initial viscosity values of S-ink and D-ink, respectively. Similar results were also observed when investigating the recovery in the oscillatory regime (Fig. 4). The S-ink and D-ink were able to recover their viscoelastic properties only after 24 h from preparation. Indeed, the G' value measured at 24 h decreased by 31% (S-ink) and 25% (D-ink), while the mean G'' loss was 56% and 22%, respectively. It is also worth noting that, in between the time points of 30 and 60 min, G' becomes higher than G'' in the two low shear amplitude windows, indicating the transition from a liquid-*like* to a solid-*like* behavior for both inks. The frequency spectra of the viscoelastic properties of S-ink and D-ink were influenced by the crosslinking kinetics (Fig. 5). Indeed, the storage moduli of the S- and D-inks were lower than the loss moduli ($\tan(\delta) > 1$, liquid-*like* condition) at 30 min after preparation, but the sol–gel transition ($G' = G''$, $\tan(\delta) = 1$) was reached between 30 min and 60 min. The viscoelastic properties of the inks were directly correlated to elapsing time, with the minimum and

Table 1 Flow behavior of the S-ink and D-ink at 30 min interpreted in terms of the power law equation parameters

Best fit parameters	S-Ink	D-Ink
n	0.12	0.51
K [Pa s^n]	59 710	9695

Table 2 Yield stress of the S-ink and D-ink. The yield point is defined as the value of shear stress where the inks transition from a solid-like behavior ($G' > G''$, $\tan(\delta) < 1$) to a liquid like one ($G' < G''$, $\tan(\delta) > 1$)

	Yield stress [Pa]	
Time	S-Ink	D-Ink
0 min	n.d.	n.d.
30 min	n.d.	n.d.
60 min	52 ± 6	87 ± 12
24 h	142 ± 10	226 ± 32

Open Access Article. Published on 26 July 2021. Downloaded on 7/12/2024 3:28:43 AM.
This article is licensed under a Creative Commons Attribution-NonCommercial 3.0 Unported Licence.

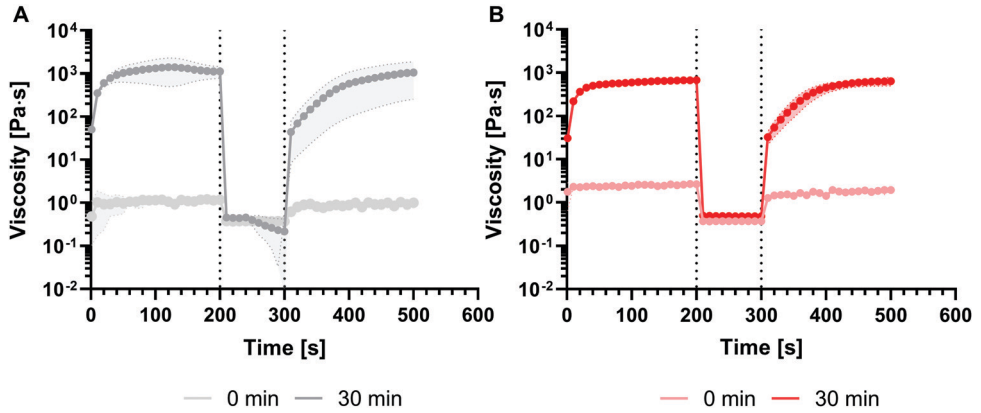

Fig. 3 Shear recovery test. A high shear rate is imposed between two low shear rate windows to simulate the extrusion process from the needle and investigate the rheological recovery of inks. In this case, the test was performed for S-ink (A) and D-ink (B) in the time points of their liquid-*like* state.

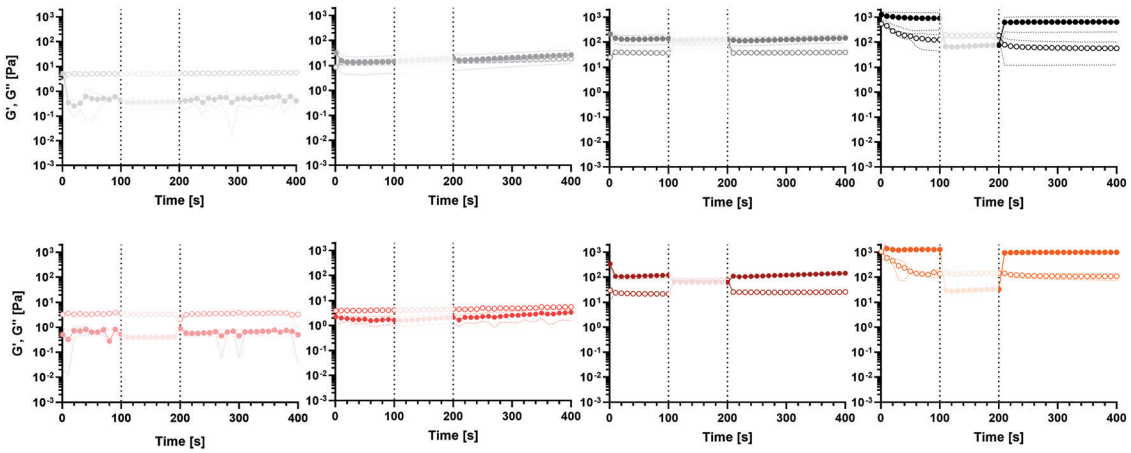

Fig. 4 *G′* (fill circles) and *G″* (empty circles) recovery after high shear amplitude simulation for S-ink and D-ink (black-shaded and red-shaded colors, respectively) at the different time points of alginate crosslinking dynamics.

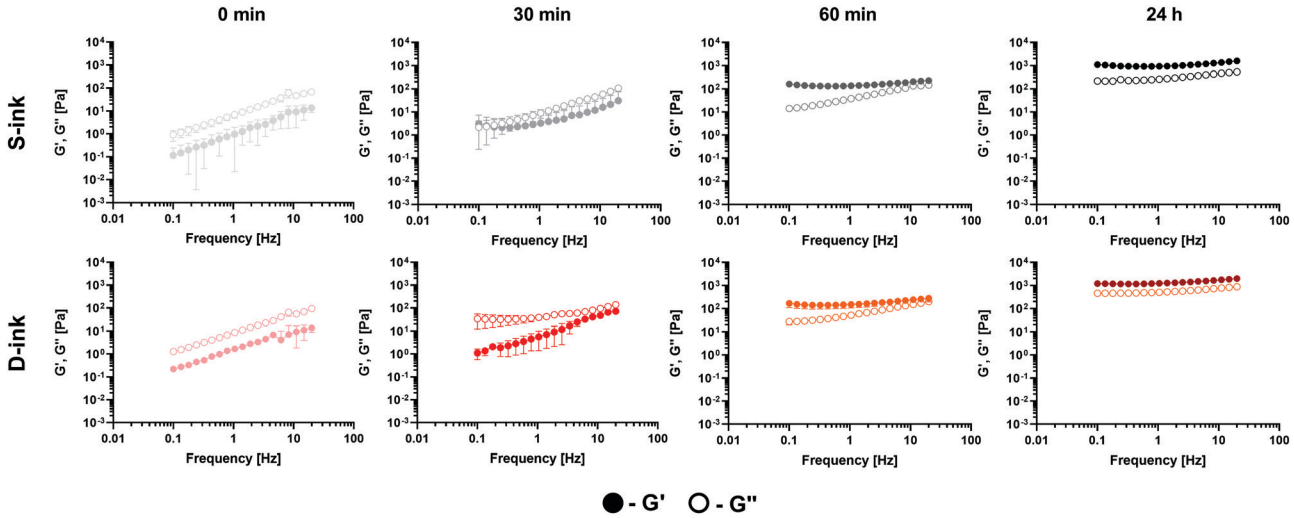

Fig. 5 Frequency response of the viscoelastic properties (*G′* and *G″*, filled and empty circles, respectively) of the S-ink (black shades) and D-ink (red shades) measured at different time points of the crosslinking dynamics.

 This journal is © The Royal Society of Chemistry 2021

Open Access Article. Published on 26 July 2021. Downloaded on 7/12/2024 3:28:43 AM.
This article is licensed under a Creative Commons Attribution-NonCommercial 3.0 Unported Licence.

maximum values of G' and G'' registered at the beginning (0 min) and completion of gelation (24 h), respectively, independently of the medium used for the preparation.

Microstructural characterisation of the inks

The frequency response of the viscoelastic properties was interpreted by applying the GMM to estimate the microstructural evolution of the inks during the gelation process.

Independently of the ink type, the estimated shear modulus and mesh size increased and decreased, respectively, with time after the gel point (Fig. 6). Indeed, for either S- or D-ink the shear modulus and mesh size were maximum and minimum, respectively, at 60 min and 24 h after preparation. Moreover, both G_∞ and ξ were not influenced by the medium used at a fixed time point.

Printability evaluation

The 3D-reactive printing of the S-ink and D-ink, which is obtained by printing the same ink at different printing times, generated fibers with features that could be strongly affected by the time between the loading into the cartridge and printing (Fig. 7). For both the ink types, the fibers were continuous for the printing processes performed in the first hour after gelation (*i.e.*, 0, 30 and 60 min), while some inhomogeneities were observed at complete gelation (t = 24 h). In this last case, the extrusion on the printing plate was characterized by the deposition of small clots of the materials.

The microscopic analysis revealed that the fiber diameter changed as a function of both time (Fig. 8A) and printing pressure (Fig. 8B and C). The 3D-reactive printing of the S-ink and D-ink showed a general decrease of the mean diameter in the first hour after preparation. Indeed, the fiber dimension was maximum immediately after printing and minimum after 60 min, independently of the pressure used for the printing procedure. For example, the fibers of the S-ink and the D-ink were, respectively, 958 ± 128 μm and 805 ± 176 μm at 0 min, and 613 ± 85 μm and 462 ± 42 μm at 60 min after preparation. The indirect relationship between fiber diameter and time was not found after 24 h, when thicker fibers were observed with respect to the other time points. Contrarily, a positive correlation was found between the dimension of the fiber and the pressure used for printing, independently of the time point and the ink. A higher pressure was required to print fibers at longer time points. For instance, the minimum pressure for S-ink was 18 kPa (20 for D-ink) at 0 min and 96 kPa (for both inks) at 24 h.

The variation of U (uniformity factor) over time confirmed the dimensional evaluation (Fig. 9A). Indeed, U was near the ideal condition (U = 1) for all the time points considered before complete gelation, with the maximum displacement from the ideal condition for the freshly prepared inks (9% and 10% for the S-ink and the D-ink, respectively). The maximum uniformity was reached after 60 min, when the real and ideal U differed only for the 1% (S-ink) and 3% (D-ink). At complete gelation, the fibers were not uniform, as the irregular deposition of the inks resulted in mean values of U that were ~66% higher than the ideal reference (maximum values over 100% in some samples, independently of the ink type).

The results of the characterization of the 3D structures, printed at different time points of the alginate gelation process, were similar to those for the single fibers: both the pore and perimeter coefficients were strongly time dependent (Fig. 9B and C). Indeed, Pr increased for both the S-ink and D-ink from values lower than 1, in the first 30 min, to values higher than unity at complete gelation. At 60 min after preparation, Pr was computed to be near the ideal condition, describing perfectly square pores (Pr = 1), with Pr equal to 1.0 ± 0.1 in both the S-ink and D-ink. Similarly, Pe showed the lowest displacement from the ideal condition (Pe = 1) after 60 min (1% and 3% for the S-ink and D-ink, respectively), as shown in the insets of Fig. 9. The highest displacement from unity was found for the freshly prepared inks: Pe = 0.95 for S-ink and Pe = 0.86 for D-ink. The means of the three parameters considered (U, Pr and Pe) were further combined in a new coefficient, defined as printability coefficient (P). Pe is a pure number, which is computed by including in eqn (8) the mean and the standard deviation of a series of printed samples.[50] As P weighs as equals the means of U and Pr with the pure value of Pe, it is also a pure number.

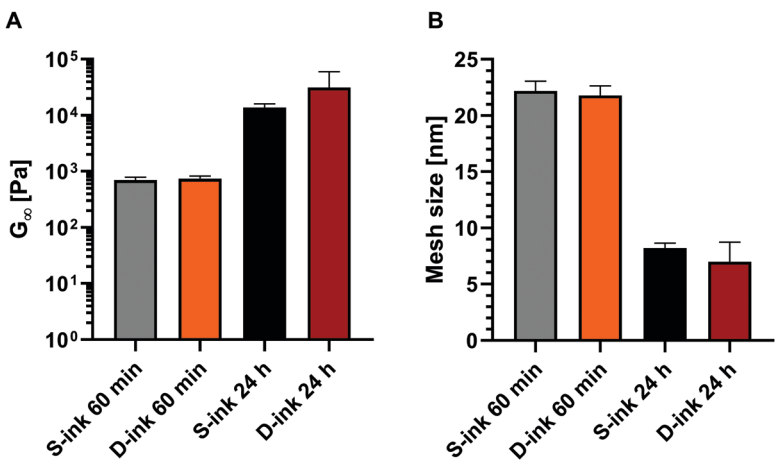

Fig. 6 Shear modulus (A) and mesh size (B) of S-ink (black shades) and D-ink (red shades) estimated at the time points of 60 min and 24 h after preparation.

Open Access Article. Published on 26 July 2021. Downloaded on 7/12/2024 3:28:43 AM.
This article is licensed under a Creative Commons Attribution-NonCommercial 3.0 Unported Licence.

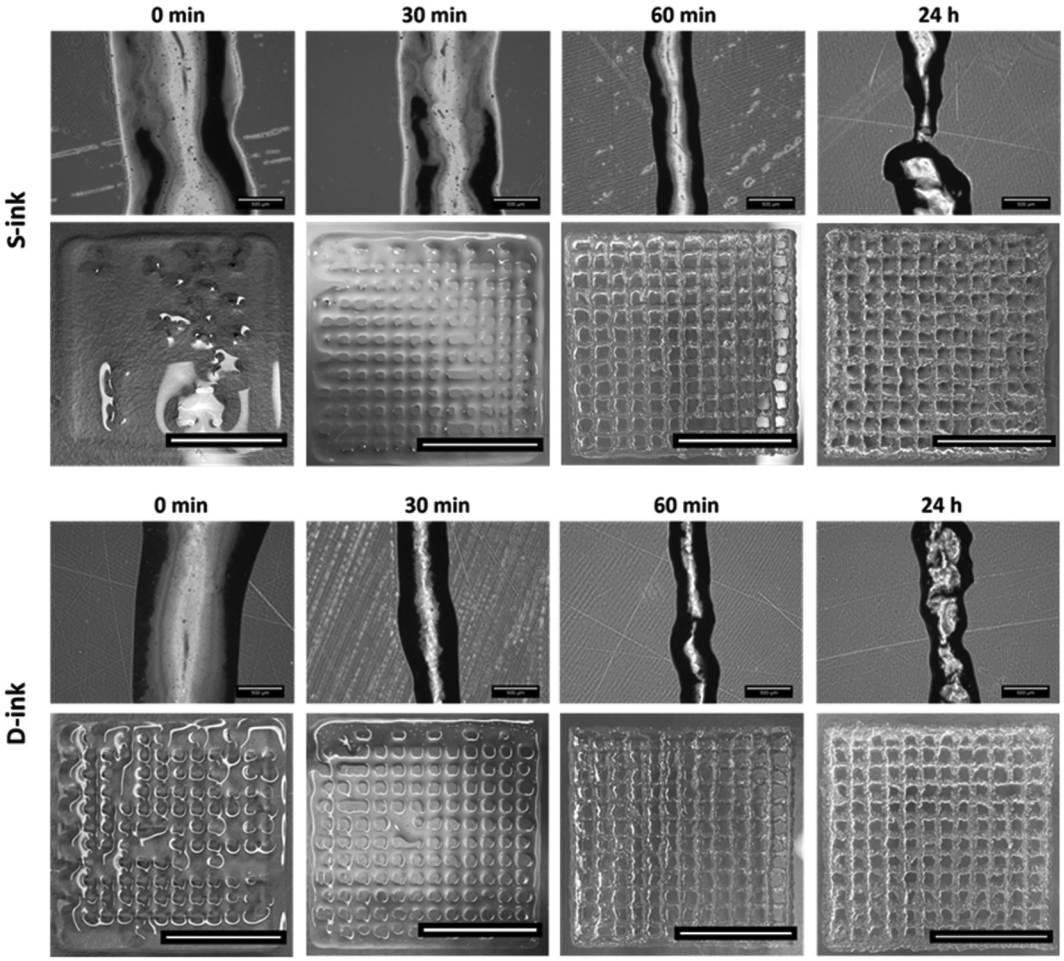

Fig. 7 The reactive printing of S-ink and D-ink. Optical microscopy of representative fibers and 3D geometries of S-ink and D-ink printed at different time points after preparation, and at a constant velocity of 15 mm s^{-1} with a nozzle of 250 μm internal diameter. The scale bar is equal to 500 μm for the fibers and 10 mm for the bi-layered geometries.

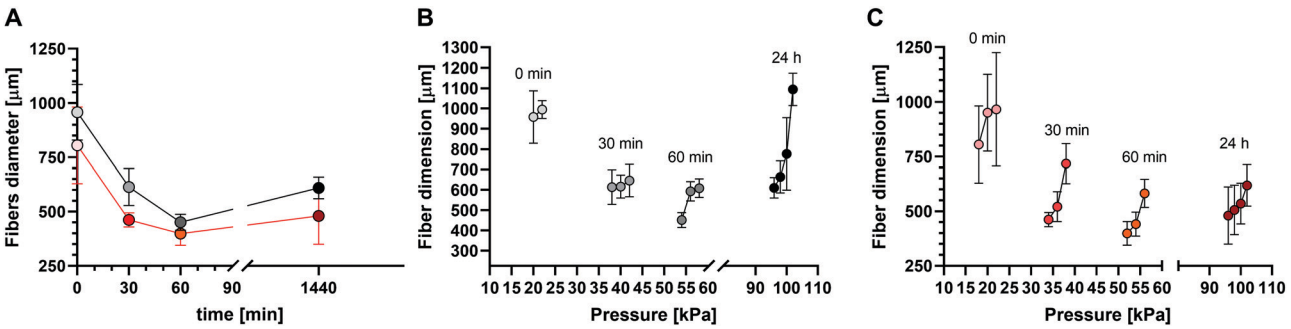

Fig. 8 Dependence of the printing results, interpreted in terms of fiber diameter, as a function of the main printing parameters, *i.e.* time (at minimal printing pressure) (A, dark shade for S-ink and red shade for D-ink) and printing pressure of S-ink and D-ink (B and C, respectively).

The ideal condition of reference was fixed, as reported in eqn (10), at the unit value (Fig. 9D):

$$P = \frac{3}{\frac{1}{\overline{U}} + \frac{1}{\overline{\mathrm{Pr}}} + \frac{1}{\mathrm{Pe}}} \quad (10)$$

P approximated the ideal value of 1 after 60 min from the preparation of S-ink and D-ink (0.99 and 0.97, respectively), with the maximum displacement found for the freshly prepared inks (10 and 20%, respectively).

Discussion

A rich state-of-the-art method was developed in the last few years for the 3D-printing of alginate hydrogels. The different

 This journal is © The Royal Society of Chemistry 2021

Open Access Article. Published on 26 July 2021. Downloaded on 7/12/2024 3:28:43 AM.
This article is licensed under a Creative Commons Attribution-NonCommercial 3.0 Unported Licence.

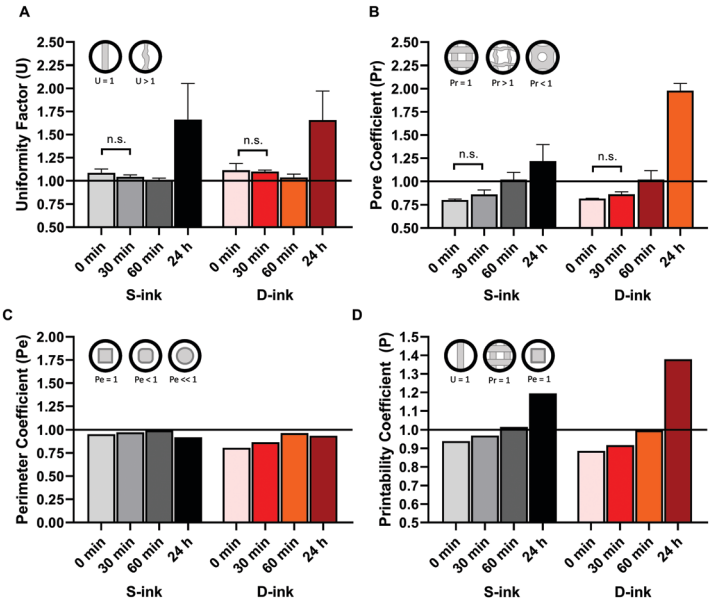

Fig. 9 Printability quantification of S-ink and D-ink (black and red shades, respectively) during the dynamics of alginate gelation. The printability is expressed in terms of four different parameters: uniformity factor (A), pore coefficient (P_r), perimeter coefficient (P_e), and their combination (printability coefficient, P) (A, B, C and D, respectively). The insets show the shape of ideal and non-ideal geometries.

techniques proposed for printing alginate inks led to many advances, such as the definition of rheological tests to investigate the ink printability and parameters for its quantification.[32,42] Recently, researchers have devoted increasing efforts to overcome one of the historical limitations observed when printing alginate, *i.e.* inhomogeneous structure of the printed fibers, by assessing new crosslinker-free inks or alternative crosslinking methods.[50,68–71] In this view, internal gelation was able to improve the homogeneity and printability of the alginate inks, while preserving some aspects of the state-of-the-art methods. For example, $CaCl_2$-baths were used to improve the shape-fidelity post extrusion even though a homogeneous crosslinking was obtained pre-printing with $CaCO_3$ and GDL.[44,50] Similarly, if $CaCO_3$ is added to the GDL solution before alginate, there is a subsequent release of free Ca^{++} prior to mixing with the polymer, recreating a condition comparable to the external gelation obtained with soluble calcium salts.[41] However, to date, the maintenance of pre- and/or post-crosslinking as a strategy for printing has not been allowed, overcoming other limitations rather than homogeneity, such as the long optimization process due to its trial-and-error nature and the necessity to adapt the process (*i.e.* printing) as a consequence of the results obtained (*i.e.* printability). In this work, we focused on changing the approach behind the whole alginate printing process by proposing the 3D-reactive printing of alginate. In this new approach, the smooth variation of the viscoelastic properties during the internal gelation process (Fig. 1) was used to tune the printability of the same ink – prepared in the same cartridge – by controlling the printing time. The acidification agent (GDL) was used to achieve comparable gel points for alginate solutions in DMEM and 0.057% NaCl by compensating for the different contributions of the components in each medium. The higher amount of GDL in the preparation of D-ink slightly reduced the pH at each time point (the maximum difference between the pH values of the two inks is equal to 8%, corresponding up to 0.5 pH units of difference). The different medium compositions of S-ink and D-ink may have influenced the crosslinking kinetics.

Indeed, time was the parameter that mainly influences the (reactive) process, as observed during either the *a priori* rheological characterization or the 3D-printing procedure. This observation was independent of the medium used for the ink preparation, *i.e.* a saline solution (0.057% w/v) (S-link) and complete DMEM (D-ink).

From a rheological point of view, the solid-*like* condition $G' > G''$ ($\tan(\delta) < 1$) was found to be a key feature to be monitored over time to select the optimized printing time. Indeed, the viscosity recovery was null for the freshly prepared S-ink and D-ink ($\tan(\delta) > 1$) and within a transitory phase of 30 min (Fig. 3). However, the solid-*like* state is not a sufficient condition for a fast recovery, as the optimized viscoelastic recovery observed in the S-ink and D-ink after 60 min from preparation ($\tan(\delta) < 1$) was not maintained after 24 h (again $\tan(\delta) < 1$). At this last time point, the increased solid-*like* behavior was experimentally associated with an increase in ink brittleness, which caused an irreversible damage during extrusion from the nozzle (Fig. 4). Remarkably, the mean values of $\tan(\delta)$ for which the S-ink and the D-ink were found to be optimally printable (60 min, $\tan(\delta)$ equal to 0.3 and 0.5, respectively) were also in good accordance with the results reported in other studies.[25,50]

The main aspects of the 3D-reactive printing process (*e.g.*, extrudability and self-standing fiber formation) were correctly predicted by rheological tests similarly to what was previously described for the state-of-the-art approaches for 3D-printing of alginate.[22,72] Printability quantification was performed by considering three parameters investigating the uniformity of

Open Access Article. Published on 26 July 2021. Downloaded on 7/12/2024 3:28:43 AM.
This article is licensed under a Creative Commons Attribution-NonCommercial 3.0 Unported Licence.

the fibers (U), shape fidelity of the 3D structure (Pr) and accordance with the theoretical perimeter (Pe).[50,73] This work proposes an additional parameter, the printability coefficient (P), thus combining in a single number the information obtained by the mean values of the previous parameters, as described using eqn (10). Similarly to the other parameters already reported in the literature, the P coefficient is equal to 1 for printed constructs that precisely resemble the CAD perimeter (Pe = 1) in well-structured 3D layers (Pr = 1) made up of perfectly straight fibers (U = 1). The printing conditions were correctly correlated with the flow behavior of the ink. Indeed, the freshly prepared S-ink and D-ink were non-printable ($P < 1$). They were immediately extruded through the nozzle when the pressure valve was moved from the minimal pressure of 18 or 20 kPa (for the S-ink and the D-ink, respectively) (Fig. 7 and 9), spreading onto the printing-plane and confirming the Newtonian behavior as well as the null recovery (Fig. 3). After 30 min, the fibers of S-ink and D-ink deposited at a velocity of 15 mm s^{-1} appeared like viscous wires and they required a higher pressure than freshly prepared inks to be extruded. The increased viscosity resulted in an improved capability to macroscopically reproduce the CAD-designed perimeter (as indicated by the Pe parameter). Although P was improved with respect to the freshly prepared inks, the slow shear recovery after the extrusion-simulated condition confirmed that the inks lacked the self-standing capability during the immediate post-printing, which resulted in poorly structured 3D networks (Fig. 9).

The high recovery ($\sim$94%) and low yield stress of the S-ink and the D-ink, printed 60 min after preparation, described a rheological analogue of the ink behavior ongoing during 3D-printing. Indeed, they were extruded in a wire-*like* shape and deposited in well-structured fibers on the support glass ($P \sim 1$). In this condition, the fibers were thinner and more continuous than those after 24 h (Fig. 7 and 9) because of the greater viscous contribution of G'', which allowed the inks to be extruded from the nozzle without breakage. Instead, after 24 h, the material laid in discontinuous blocks, resulting in non-uniform fibers ($U \gg 1$) due to hydrogel fragmentation during the extrusion. This fact was correctly indicated by the ink breakage during the high shear strain window of the viscoelastic recovery test and the resulting G' decay.

The 3D-reactive printing approach brought at least two advantages. First, it produced structures more adherent to the designed geometry than those obtained by internal gelation without monitoring the time properties of the ink. For example, the spreading ratio (*i.e.*, fiber diameter/nozzle diameter) of the S-ink and the D-ink, at the optimized time point of 60 min, was found to be 44–62% lower than those of other inks with comparable compositions but printed without investigating the optimal printing time.[41] Second, the 3D-reactive printing of alginate showed the potential to engineer in one single step what was typically produced with the pre- and/or post-crosslinking approach in terms of fiber diameter, uniformity and printability.[44,50]

The well-assessed rheological characterization used to simplify the optimization process of the ink is not able, alone, to allow a deep investigation of the microstructure of the ink itself. However, this parameter affects the diffusion of molecules, such as oxygen, nutrients and other molecules, and their availability for the cells in the fibers, modulating in this way their growth.[63,74,75] It is, hence, of primary importance to combine the dimensional characterization of the printing fibers with the estimation of their microstructure in the perspective of cellular studies. For this reason, the characterization for the printability investigation was enriched with the rheological approach already used to estimate the hydrogel microstructure in other applications.[63,76]

In this work, the GMM was used to fit the frequency spectra of the S-ink and the D-ink, thus estimating the shear modulus (G_∞) and mesh size (ξ), which are indicators of their resistance to shear deformation and the distance between two crosslinking sites on the same alginate chain, respectively.[66]

The possibility of characterizing *a priori* the internal microstructure of the fibers could allow, for example, investigating the cell behavior *a posteriori* of the printing process by defining suitable computational models, as already proposed in other studies not focused on 3D-printing.[61] Similarly, microstructural characterization could also be used to preliminarily investigate the suitability of the ink for cellular studies by comparing the estimated mesh size with literature data. For example, the mesh sizes of S-ink and D-ink were comparable to those found to facilitate oxygen and glucose diffusion in hydrogels seeded with human adipose-derived stem cells, with a cellular availability of $\sim$80%.[74] This would boost the minimization of the waste of resources, by facilitating *a priori* the recognition of critical cellular applications or, conversely, of optimal culture parameters when available in the literature.

Thanks to the mesh size estimation, it was possible to further monitor the hydrogel networks after the gel point. Following the theory (eqn (5)), the mesh size was inversely proportional to the shear modulus and coherent with the gelation process pictured during the time sweep test. Indeed, the number of crosslinking sites increased over time due to the increasing availability of calcium ions after GDL addition, leading to a continuous reduction of the network microstructure.[66] The mesh size reduction (7 ± 2 and 8 ± 1 nm for S- ink and D-ink, respectively) ended after 24 h, when gelation was completed, and was found to be comparable (3–10 nm) to other alginate hydrogels with similar polymer concentrations.[64,76]

It is also worth noting that the method proposed for the microstructure estimation may not be similarly suitable neither for externally crosslinked inks nor for internally pre-crosslinked and externally post-crosslinked hydrogels. Indeed, the estimation obtained by combining the GMM with the rubber elasticity theory assumes a homogeneous network formation, a condition which is hardly met for the well-assessed $CaCl_2$-mediated printing methods.[37,66]

Conclusions

The 3D-reactive printing of alginate produced self-standing fibers with a defined shape after extrusion, without the addition of additives. All the controlling parameters affecting the reaction

 This journal is © The Royal Society of Chemistry 2021

Open Access Article. Published on 26 July 2021. Downloaded on 7/12/2024 3:28:43 AM.
This article is licensed under a Creative Commons Attribution-NonCommercial 3.0 Unported Licence.

kinetics should be carefully considered. For example, it was demonstrated that medium composition plays a role in the ionic crosslinking kinetics of alginate. On the other hand, the controlling factors are important tools that can be used to optimize the reactive inks. In our specific case, 3D-reactive printing of both S-ink and D-ink showed the highest printability coefficient after 60 min from preparation.

The proposed method allows engineering of the mechanism of alginate gelation, moving from an immediate crosslinking to a progressive one. This is a considerable shift of the state-of-art of 3D-printed alginate hydrogels, which implies pre-crosslinked or post-crosslinked alginate solutions. In line of principle, the 3D-reactive printing, here applied for alginate, may be extended to other materials that can be crosslinked by reactions with predetermined and controllable kinetics. This opens the possibility of switching the typical approach of adapting the hydrogels to the process to the adaptation of the process to the hydrogels.

Coupled with *ad hoc* rheological characterization, 3D-reactive printing opens the possibility of identifying a time window to make a previously unprintable ink printable. This influences its uses in the thriving field of 3D-printing for cell-based bioengineering applications.

Author contributions

L. S. and P. P. conceived the main conceptual idea; all authors planned the experiments; L. S. performed the experiments with the support of M. T.; F. B. V. carried out the rheological characterization. L. S. analysed the data under the supervision of F. B. V. and wrote the original draft; all authors revised the manuscript; M. T., F. B. V. and P. P. funded the research. All authors have read and approved the version of the manuscript to be published.

Conflicts of interest

There are no conflicts to declare.

Acknowledgements

This work received funding from Fondazione Cariplo (Grant no: 2019-4615, NeuroID). We thank Prof. Sara Mantero for the constructive support and useful discussion. We are also grateful to the Research Office (Politecnico di Milano) for administrative support.

References

1 Z. Zhu, D. W. H. Ng, H. S. Park and M. C. McAlpine, 3D-printed multifunctional materials enabled by artificial-intelligence-assisted fabrication technologies, *Nat. Rev. Mater.*, 2021, **6**, 27–47.
2 F. Craveiro, S. Nazarian, H. Bartolo, P. J. Bartolo and J. Pinto Duarte, An automated system for 3D printing functionally graded concrete-based materials, *Addit. Manuf.*, 2020, **33**, 101146.
3 T. A. M. Salet, Z. Y. Ahmed, F. P. Bos and H. L. M. Laagland, Design of a 3D printed concrete bridge by testing, *Virtual Phys. Prototyping.*, 2018, **13**, 222–236.
4 S. Caulier, E. Doets and M. Noort, An exploratory consumer study of 3D printed food perception in a real-life military setting, *Food Qual. Prefer.*, 2020, **86**, 104001.
5 A. Ambrosi and M. Pumera, 3D-printing technologies for electrochemical applications, *Chem. Soc. Rev.*, 2016, **45**, 2740–2755.
6 K. Sun, *et al.*, 3D printing of interdigitated Li-ion microbattery architectures, *Adv. Mater.*, 2013, **25**, 4539–4543.
7 R. Xiao, *et al.*, 3D printing of titanium-coated gradient composite lattices for lightweight mandibular prosthesis, *Composites, Part B*, 2020, **193**, 108057.
8 O. Rungrojwittayakul, *et al.*, Accuracy of 3D Printed Models Created by Two Technologies of Printers with Different Designs of Model Base, *J. Prosthodontics*, 2020, **29**, 124–128.
9 A. A. Giannopoulos, *et al.*, Applications of 3D printing in cardiovascular diseases, *Nat. Rev. Cardiol.*, 2016, **13**, 701–718.
10 J. Kwon, *et al.*, Modelling and manufacturing of 3D-printed, patient-specific, and anthropomorphic gastric phantoms: a pilot study, *Sci. Rep.*, 2020, **10**, 1–11.
11 R. Mazrouei, V. Velasco and R. Esfandyarpour, 3D-bioprinted all-inclusive bioanalytical platforms for cell studies, *Sci. Rep.*, 2020, **10**, 1–11.
12 G. D. M. Jeffries, *et al.*, 3D micro-organisation printing of mammalian cells to generate biological tissues, *Sci. Rep.*, 2020, **10**, 1–10.
13 B. N. Johnson, *et al.*, 3D printed nervous system on a chip, *Lab Chip*, 2016, **16**, 1393–1400.
14 N. Mukherjee, A. Adak and S. Ghosh, Recent trends in the development of peptide and protein-based hydrogel therapeutics for the healing of CNS injury, *Soft Matter*, 2020, **16**, 10046–10064.
15 F. Pati, *et al.*, Ornamenting 3D printed scaffolds with cell-laid extracellular matrix for bone tissue regeneration, *Biomaterials*, 2015, **37**, 230–241.
16 L. Sardelli, *et al.*, Engineering biological gradients, *J. Appl. Biomater. Funct. Mater.*, 2019, **17**, 1–15.
17 D. H. Rosenzweig, E. Carelli, T. Steffen, P. Jarzem and L. Haglund, 3D-printed ABS and PLA scaffolds for cartilage and nucleus pulposustissue regeneration, *Int. J. Mol. Sci.*, 2015, **16**, 15118–15135.
18 S. Baiguera, *et al.*, 3D Printing Decellularized Extracellular Matrix to Design Biomimetic Scaffolds for Skeletal Muscle Tissue Engineering, *BioMed Res. Int.*, 2020, **2020**, 1–13.
19 I. T. Ozbolat and M. Hospodiuk, Current advances and future perspectives in extrusion-based bioprinting, *Biomaterials*, 2016, **76**, 321–343.
20 C. Mandrycky, Z. Wang, K. Kim and D. H. Kim, 3D bioprinting for engineering complex tissues, *Biotechnol. Adv.*, 2016, **34**, 422–434.
21 S. C. Lee, G. Gillispie, P. Prim and S. J. Lee, Physical and Chemical Factors Influencing the Printability of Hydrogel-based Extrusion Bioinks, *Chem. Rev.*, 2020, **120**, 10834–10886.

Open Access Article. Published on 26 July 2021. Downloaded on 7/12/2024 3:28:43 AM.
This article is licensed under a Creative Commons Attribution-NonCommercial 3.0 Unported Licence.

22 N. Paxton, *et al.*, Proposal to assess printability of bioinks for extrusion-based bioprinting and evaluation of rheological properties governing bioprintability, *Biofabrication*, 2017, **9**, 044107.
23 L. D. Loozen, F. Wegman, F. C. Öner, W. J. A. Dhert and J. Alblas, Porous bioprinted constructs in BMP-2 non-viral gene therapy for bone tissue engineering, *J. Mater. Chem. B*, 2013, **1**, 6619–6626.
24 J. M. Townsend, E. C. Beck, S. H. Gehrke, C. J. Berkland and M. S. Detamore, Flow behavior prior to crosslinking: The need for precursor rheology for placement of hydrogels in medical applications and for 3D bioprinting, *Prog. Polym. Sci.*, 2019, **91**, 126–140.
25 T. Gao, *et al.*, Optimization of gelatin–alginate composite bioink printability using rheological parameters: a systematic approach, *Biofabrication*, 2018, **10**, 034106.
26 S. Joas, G. Tovar, O. Celik, C. Bonten and A. Southan, Extrusion-Based 3D Printing of Poly(ethylene glycol) Diacrylate Hydrogels Containing Positively and Negatively Charged Groups, *Gels*, 2018, **4**, 69.
27 E. Gioffredi, *et al.*, Pluronic F127 Hydrogel Characterization and Biofabrication in Cellularized Constructs for Tissue Engineering Applications, *Procedia CIRP*, 2016, **49**, 125–132.
28 S. S. Ramirez Caballero, *et al.*, 3-D printing of chitosan-calcium phosphate inks: rheology, interactions and characterization, *J. Mater. Sci.: Mater. Med.*, 2019, **30**, 6.
29 A. Tocchio, *et al.*, Versatile fabrication of vascularizable scaffolds for large tissue engineering in bioreactor, *Biomaterials*, 2015, **45**, 124–131.
30 C. E. Campiglio, *et al.*, Cross-linking optimization for electrospun gelatin: Challenge of preserving fiber topography, *Polymers*, 2020, **12**, 1–15.
31 W. Lee, *et al.*, Multi-layered culture of human skin fibroblasts and keratinocytes through three-dimensional freeform fabrication, *Biomaterials*, 2009, **30**, 1587–1595.
32 P. Rastogi and B. Kandasubramanian, Review of alginate-based hydrogel bioprinting for application in tissue engineering, *Biofabrication*, 2019, **11**, 042001.
33 Y. Shao, D. Chaussy, P. Grosseau and D. Beneventi, Use of Microfibrillated Cellulose/Lignosulfonate Blends as Carbon Precursors: Impact of Hydrogel Rheology on 3D Printing, *Ind. Eng. Chem. Res.*, 2015, **54**, 10575–10582.
34 J. Wang, *et al.*, 3D printed agar/calcium alginate hydrogels with high shape fidelity and tailorable mechanical properties, *Polymer*, 2020, **214**, 123238, DOI: 10.1016/j.polymer.2020.123238.
35 C. C. Piras and D. K. Smith, Multicomponent polysaccharide alginate-based bioinks, *J. Mater. Chem. B*, 2020, **8**, 8171–8188.
36 R. E. Abouzeid, *et al.*, In situ mineralization of nano-hydroxyapatite on bifunctional cellulose nanofiber/polyvinyl alcohol/sodium alginate hydrogel using 3D printing, *Int. J. Biol. Macromol.*, 2020, **160**, 538–547.
37 G. Kaklamani, D. Cheneler, L. M. Grover, M. J. Adams and J. Bowen, Mechanical properties of alginate hydrogels manufactured using external gelation, *J. Mech. Behav. Biomed. Mater.*, 2014, **36**, 135–142.
38 J. M. C. Puguan, X. Yu and H. Kim, Characterization of structure, physico-chemical properties and diffusion behavior of Ca-Alginate gel beads prepared by different gelation methods, *J. Colloid Interface Sci.*, 2014, **432**, 109–116.
39 M. Borgogna, G. Skjåk-Bræk, S. Paoletti and I. Donati, On the initial binding of alginate by calcium ions. the tilted egg-box hypothesis, *J. Phys. Chem. B*, 2013, **117**, 7277–7282.
40 S. Naghieh, M. R. Karamooz-Ravari, M. D. Sarker, E. Karki and X. Chen, Influence of crosslinking on the mechanical behavior of 3D printed alginate scaffolds: Experimental and numerical approaches, *J. Mech. Behav. Biomed. Mater.*, 2018, **80**, 111–118.
41 F. E. Freeman and D. J. Kelly, Tuning alginate bioink stiffness and composition for controlled growth factor delivery and to spatially direct MSC Fate within bioprinted tissues, *Sci. Rep.*, 2017, **7**, 1–12.
42 J. H. Y. Chung, *et al.*, Bio-ink properties and printability for extrusion printing living cells, *Biomater. Sci.*, 2013, **1**, 763–773.
43 I. Fernández Farrés and I. T. Norton, Formation kinetics and rheology of alginate fluid gels produced by in-situ calcium release, *Food Hydrocolloids*, 2014, **40**, 76–84.
44 S. Liu, *et al.*, Bioactive and Biocompatible Macroporous Scaffolds with Tunable Performances Prepared Based on 3D Printing of the Pre-Crosslinked Sodium Alginate/Hydroxyapatite Hydrogel Ink, *Macromol. Mater. Eng.*, 2019, **304**, 1–11.
45 C. K. Kuo and P. X. Ma, Ionically crosslinked alginate hydrogels as scaffolds for tissue engineering: Part 1. Structure, gelation rate and mechanical properties, *Biomaterials*, 2001, **22**, 511–521.
46 E. Amici, G. Tetradis-Meris, C. P. de Torres and F. Jousse, Alginate gelation in microfluidic channels, *Food Hydrocolloids*, 2008, **22**, 97–104.
47 D. Poncelet, *et al.*, Production of alginate beads by emulsification/internal gelation. I. Methodology, *Appl. Microbiol. Biotechnol.*, 1992, **38**, 39–45.
48 S. Mokhtari, S. M. Jafari and E. Assadpour, Development of a nutraceutical nano-delivery system through emulsification/internal gelation of alginate, *Food Chem.*, 2017, **229**, 286–295.
49 C. M. Silva, A. J. Ribeiro, I. V. Figueiredo, A. R. Gonçalves and F. Veiga, Alginate microspheres prepared by internal gelation: Development and effect on insulin stability, *Int. J. Pharm.*, 2006, **311**, 1–10.
50 J. Hazur, *et al.*, Improving alginate printability for biofabrication: establishment of a universal and homogeneous pre-crosslinking technique, *Biofabrication*, 2020, **12**, 045004.
51 I. T. Ozbolat, H. Chen and Y. Yu, Development of 'Multi-arm Bioprinter' for hybrid biofabrication of tissue engineering constructs, *Robot. Comput. Integr. Manuf.*, 2014, **30**, 295–304.
52 S. Ahn, H. Lee, L. J. Bonassar and G. Kim, Cells (MC3T3-E1)-laden alginate scaffolds fabricated by a modified solid-freeform fabrication process supplemented with an aerosol spraying, *Biomacromolecules*, 2012, **13**, 2997–3003.
53 H. Li, Y. J. Tan, R. Kiran, S. B. Tor and K. Zhou, Submerged and non-submerged 3D bioprinting approaches for the fabrication of complex structures with the hydrogel pair GelMA and alginate/methylcellulose, *Addit. Manuf.*, 2020, **37**(8), 101640, DOI: 10.1016/j.addma.2020.101640.

 This journal is © The Royal Society of Chemistry 2021

Open Access Article. Published on 26 July 2021. Downloaded on 7/12/2024 3:28:43 AM.
This article is licensed under a Creative Commons Attribution-NonCommercial 3.0 Unported Licence.

54 W. Liu, *et al.*, Coaxial extrusion bioprinting of 3D microfibrous constructs with cell-favorable gelatin methacryloyl microenvironments, *Biofabrication*, 2018, **10**, 024102.
55 N. Taira, K. Ino, J. Robert and H. Shiku, Electrochemical printing of calcium alginate/gelatin hydrogel, *Electrochim. Acta*, 2018, **281**, 429–436.
56 G. Skjåk-Bræk, H. Grasdalen and O. Smidsrød, Inhomogeneous polysaccharide ionic gels, *Carbohydr. Polym.*, 1989, **10**, 31–54.
57 G. Marchioli, *et al.*, Fabrication of three-dimensional bioplotted hydrogel scaffolds for islets of Langerhans transplantation, *Biofabrication*, 2015, **7**, 025009.
58 B. M. Baker and C. S. Chen, Deconstructing the third dimension-how 3D culture microenvironments alter cellular cues, *J. Cell Sci.*, 2012, **125**, 3015–3024.
59 B. Stokke, Polysaccharide Hydrogels, *Gels*, 2019, **5**, 38.
60 H. Suhaimi, S. Wang, T. Thornton and D. B. Das, On glucose diffusivity of tissue engineering membranes and scaffolds, *Chem. Eng. Sci.*, 2015, **126**, 244–256.
61 F. Qu, *et al.*, Maturation State and Matrix Microstructure Regulate Interstitial Cell Migration in Dense Connective Tissues, *Sci. Rep.*, 2018, **8**, 1–13.
62 P. Muller, Glossary of terms used in physical organic chemistry (IUPAC Recommendations 1994), *Pure Appl. Chem.*, 1994, **66**, 1077–1184.
63 D. P. Pacheco, *et al.*, Disassembling the complexity of mucus barriers to develop a fast screening tool for early drug discovery, *J. Mater. Chem. B*, 2019, **7**, 4940–4952.
64 G. Turco, *et al.*, Mechanical spectroscopy and relaxometry on alginate hydrogels: A comparative analysis for structural characterization and network mesh size determination, *Biomacromolecules*, 2011, **12**, 1272–1282.
65 L. Sardelli, *et al.*, Towards bioinspired in vitro models of intestinal mucus, *RSC Adv.*, 2019, **9**, 15887–15899.
66 P. Matricardi, F. Alhaique and T. Coviello, *Polysaccharide Hydrogels*, 2016.
67 A. Bonfanti, J. L. Kaplan, G. Charras and A. Kabla, Fractional viscoelastic models for power-law materials, *Soft Matter*, 2020, **16**, 6002–6020.
68 M. T. I. Mredha, V. T. Tran, S. G. Jeong, J. K. Seon and I. Jeon, A diffusion-driven fabrication technique for anisotropic tubular hydrogels, *Soft Matter*, 2018, **14**, 7706–7713.
69 Y. Sümbelli, *et al.*, In situand non-cytotoxic cross-linking strategy for 3D printable biomaterials, *Soft Matter*, 2021, **17**, 1008–1015.
70 X. Zhang, *et al.*, Crosslinker-free silk/decellularized extracellular matrix porous bioink for 3D bioprinting-based cartilage tissue engineering, *Mater. Sci. Eng., C*, 2021, **118**, 111388.
71 Y. P. Singh, A. Bandyopadhyay and B. B. Mandal, 3D Bioprinting Using Cross-Linker-Free Silk-Gelatin Bioink for Cartilage Tissue Engineering, *ACS Appl. Mater. Interfaces*, 2019, **11**, 33684–33696.
72 T. Gao, *et al.*, Optimization of gelatin-alginate composite bioink printability using rheological parameters: A systematic approach, *Biofabrication*, 2018, **10**, 034106.
73 L. Ouyang, R. Yao, Y. Zhao and W. Sun, Effect of bioink lproperties on printability and cell viability for 3D bioplotting of embryonic stem cells, *Biofabrication*, 2016, **8**, 035020.
74 L. Figueiredo, *et al.*, Assessing glucose and oxygen diffusion in hydrogels for the rational design of 3D stem cell scaffolds in regenerative medicine, *J. Tissue Eng. Regener. Med.*, 2018, **12**, 1238–1246.
75 J. Malda, *et al.*, Oxygen Gradients in Tissue-Engineered PEGT/PBT Cartilaginous Constructs: Measurement and Modeling, *Biotechnol. Bioeng.*, 2004, **86**, 9–18.
76 M. Grassi, *et al.*, Structural Characterization of Calcium Alginate Matrices by Means of Mechanical and Release Tests, *Molecules*, 2009, **14**, 3003–3017.